Isoscalar breathing mode state in ^{90}Zr and ^{116}Sn

C. M. Rozsa, D. H. Youngblood, J. D. Bronson, Y.-W. Lui, and U. Garg

Cyclotron Institute, Texas A&M University, College Station, Texas 77843

Beams of 96- and 129-MeV α particles were used to excite the giant resonance region in ^{90}Zr and ^{116}Sn. From the analysis of data obtained from 0° to 8°, two distinct components of the giant resonance peak were resolved in each nucleus. The upper component is well described by a distorted-wave Born-approximation calculation for $L = 0$ exhausting 90% (180%) of the energy weighted sum rule and has $E_x = 16.2$ MeV (15.6 MeV), $\Gamma = 3.5$ MeV (4.1 MeV) for ^{90}Zr (^{116}Sn). The nuclear incompressibility is extracted from these data and from that available for ^{144}Sm and ^{208}Pb. The lower component is the giant quadrupole resonance exhausting 66% (84%) of the isoscalar quadrupole sum rule and has $E_x = 14.0$ MeV (13.2 MeV), $\Gamma = 3.4$ MeV (3.3 MeV) for ^{90}Zr (^{116}Sn).

$$\left[\begin{array}{l}\text{NUCLEAR REACTIONS } ^{90}\text{Zr, } ^{116}\text{Sn}(\alpha, \alpha'), \ E_\alpha = 96, 129 \text{ MeV. Measured } E_x, \\ \quad \sigma(\theta), \text{ giant resonances; deduced } L, \beta, \text{ nuclear incompressibility.}\end{array}\right]$$

I. INTRODUCTION

The hydrodynamical model of the nucleus predicts fundamental modes of vibration, commonly referred to as giant resonances. Among the modes which have been investigated are the isovector giant dipole resonance (GDR) ($J^\pi = 1^-$), which is the most well known, and the isoscalar giant quadrupole resonance (GQR) ($J^\pi = 2^+$); the properties of these modes are known for many nuclei. The isoscalar giant monopole resonance (GMR) ($J^\pi = 0^+$), also referred to as the breathing mode state, has only recently been identified and is of great interest because its energy is directly related[1,2] to the incompressibility of nuclear matter.

Definitive evidence for the existence of the GMR has come from our measurements[3] at small angles of α particles inelastically scattered from ^{144}Sm and ^{208}Pb. A distinctive minimum exists in the angular distribution (at about 4°) for a monopole state which is absent for other multipolarities. In this paper, extensions of these measurements to 0°, where the cross section for the GMR is a maximum, are reported, and strong evidence is presented for the existence of the GMR in ^{90}Zr and ^{116}Sn. The incompressibility of nuclear matter is extracted from the location of the GMR and is compared to random-phase approximation (RPA) predictions.

II. EXPERIMENTAL PROCEDURE

Beams of 96- and 129-MeV α particles from the Texas A&M cyclotron were energy analyzed by a 165° magnet to ~50-keV energy spread. The targets of ^{90}Zr and ^{116}Sn were self-supported, isotopically enriched ($>$95%) metal foils with thicknesses of 4.0 and 6.3 mg/cm^2, respectively. Inelastically scattered α particles were detected over an energy range of 65 MeV with a 1.2-cm-high by 86-cm-long resistive wire proportional counter in the focal plane of an Enge split-pole magnetic spectrograph. An overall energy resolution of approximately 300 keV was obtained. The proportional counter was backed by an NE102 scintillator to provide total energy, as well as time-of-flight signals obtained relative to the cyclotron rf. Energy loss signals from both ends of the proportional counter ($\Delta E_1, \Delta E_2$) and the total energy signal (E) were routed through analog-to-digital converters (ADC) to the PDP-15 computer after appropriate amplification and shaping; time-of-flight signals (TOF) went directly from a time-to-amplitude converter to an ADC. The ADC's were gated, and the computer accepted an event only when all four signals were present. Signals from the proportional counter were routed through a pileup inspector, and only events separated by more than 4 μsec were accepted. To obtain accurate dead times, CAMAC scalers counted the number of events rejected by the pileup inspector and the number rejected while data were being processed by the ADC's and the computer.

A data acquisition program was constructed to maximize available counting rates while allowing proper particle identification over the full length of the counter. Both $\Delta E_T = \Delta E_1 + \Delta E_2$ and position $P = \Delta E_1 / \Delta E_T$ were calculated for each event. The pulse heights for ΔE and E were found to vary linearly with position; this could be observed in two dimensional arrays (ΔE vs P and E vs P) stored in memory. Corrected pulse heights, $\Delta E_T'$ and E', independent of position were obtained by applying a linear correction. The resulting $\Delta E_T'$

and E', as well as the TOF events, were stored in singles arrays.

Particle identification was obtained by setting software gates on spectra corresponding to the energy loss ($\Delta E'_T$) in the proportional counter, total energy deposited (E') in the scintillator, and time-of-flight. Only alpha particles, protons, and deuterons had significant yield in the region of interest in the spectra (below $E_x \sim 40$ MeV). Although the $\Delta E'_T$ gate alone was able to remove essentially all unwanted events, the E' and TOF gates were maintained for additional discrimination. Two sets of these gates could be set to collect data in different exit channels. Three 2048 channel position arrays were stored in core, one into which all incoming signals were routed, the second and third corresponding to those events which satisfy conditions on $\Delta E'_T$, E', and TOF. The α spectrum was stored in the second position array and (usually) the ^{3}He spectrum in the third. With the use of three large data buffers, data could be processed at about a 3 kHz average rate without significant losses.

An energy (momentum) calibration over the entire range of the proportional counter was obtained from the ^{12}C(α, α')^{12}C and ^{12}C($\alpha, ^3$He)^{13}C reactions taken at several angles. Generally, elastically scattered α particles impinged near the high ρ end of the counter, while outgoing ^{3}He particles were observed near the low ρ end. The beam energy was calibrated with an analog H$_2^+$ beam ($E_p \sim \frac{1}{4}E_\alpha$) by comparing the relative positions[4] of peaks from ^{24}Mg(p, p') and ^{24}Mg(p, d) reactions with a thin ($\sim$150 μg/cm^2) Mg foil enriched to 95% in ^{24}Mg. The scattering angle was checked by measuring the crossover of the H(p, p)H with ^{24}Mg(p, p')^{24}Mg* (1.37 MeV). During routine runs, both beam energy and scattering angle were checked by comparing the relative positions of ^{12}C(α, α'), ^{12}C($\alpha, ^3$He), H(α, α'), and H($\alpha, ^3$He)d lines in the spectra.

Collection of data in the inelastic channel at small angles required careful preparation of the slits in both the beam line and the spectrograph, and proper tuning of the beam optics elements to remove (or minimize) spurious events. If the beam was not properly tuned or cleanup slits not properly set, secondary components could exist in the beam that appeared as peaks $\sim$1–10 MeV wide in the α spectrum with up to $\sim$30-MeV energy loss. These could be directly observed by looking up the beam line with no target in place. Particles elastically scattered from the target which struck the edge of the solid-angle defining slits produced "continuum-like" background throughout the spectrum. This spectrum was easily observed with a high Z target (such as Pb) by moving the focal

plane counter vertically to a position where real events from the target were absent.

In order to minimize spurious contributions from the beam, one set of slits was used to restrict the phase space of the beam before it entered the 165° analyzing magnet, and three sets were used to clean up the beam after the analyzing magnet. One set was placed at a beam focus between the analyzing magnet and a 5° switching magnet; two sets were placed at foci between the switching magnet and the spectrograph.

To minimize scattering from slits, both the beam cleanup and the solid-angle defining slits were made of brass just of sufficient thickness to stop the beam particles, and the edges were polished to a mirror finish (see Ref. 5). We obtained best results with slits that had a flat edge and slightly rounded corners. The beam cleanup slits after the analyzing magnet and the solid-angle defining slits at the spectrograph entrance were prepared in this way. The energy-defining slits at the exit of the 165° analyzing magnet were made from Ta with an edge just thick enough to stop the beam particles. The rest of the slit was made thicker ($\times$2) to stop or attenuate the p, d, and t produced in the slits.

Beam preparation proceeded as follows. A visually aberration-free spot, typically 1 mm high by 2 mm wide, was obtained at the target with the beam cleanup slits open. Then with the spectrograph positioned at a small angle (typically $\sim$1.7°) where extraneous particles coming down the beam line (but not the primary beam) could enter the spectrograph, the spectrum was observed with no target in place. Generally, a large counting rate of α particles with energy only slightly below that of the beam was present; the three sets of beam cleanup slits were then positioned to remove these pseudobeam events. When the cleanup slits were allowed to cut the primary beam, strong broad peaks appeared in the spectrum. In practice, there was a fairly wide range of settings for each slit which removed the pseudobeam events but did not produce other observable background. The counting rate in the detector after the above process was completed was negligible compared to the inelastic rate at any angle with a target in place. As a further check, the spectrograph was moved to 0° and the beam was allowed to enter the spectrograph but was stopped just before the detector. The spectrum with no target in place had to be smooth and have a small overall rate (generally < 100 events/sec for $\sim$10 nA of beam).

The small angle measurements (but not 0°) used a double slit made of copper at the entrance to the spectrograph. The first set had a solid angle of 0.6°$\times$1.6°, while the second had a somewhat

larger opening and served to catch some particles scattered from the first set. For measurements at 0°, the beam was passed into the spectrograph and one set of brass defining slits with an opening of 6.4° horizontally by 3.7° vertically was used. For light targets ($A \lesssim 40$), clean spectra were obtained at 0° with the normal 3° horizontal by 1.5° vertical opening into the Enge split-pole spectrograph; for heavy targets the large number of elastic events impinging upon the edges of the solid-angle defining slits produced a large smooth background in the focal plane counter. Opening the solid-angle defining slits decreased slit scattering contributions, primarily through the reduction of elastic events ($\sigma_R \alpha \sin^{-4}\theta$) hitting slit edges, but also because the solid angle of the slit edges compared to the slit opening was reduced. Opening the slits well beyond 3° by 1.5° increases aberrations, and could result in particles striking the magnet pole tips. The most effective settings were obtained empirically by opening the slits individually and measuring the ratio of the ^{3}He yield from ^{208}Pb(α, ^{3}He) reaction to the continuum α yield. A broad maximum was apparent in the yield of real events (^{3}He) relative to the yield of alpha particles scattered from the solid-angle defining slits. A careful calibration of the effective solid angle at 0° was then required and is described later.

Three different Faraday cups were necessary in different angle ranges for current integration. For measurements at 0°, a thick Ta plate with its edge milled at 45° to the focal plane (parallel to the central rays crossing the focal plane) was placed immediately in front of the focal plane detector and served as a Faraday cup. It could be moved parallel to the focal plane to prevent the beam from entering the focal plane detector. At angles other than 0°, this Faraday cup blocked elastically scattered particles from the detector. For angles 1.5° to 4.5°, a Ta plate attached to the first of the copper slits of the double slit insert described above was used as a Faraday cup. The third Faraday cup was a curved Ta plate that was positioned to intercept the beam when data were taken at angles $\geqslant 5°$; its edge was kept at a minimum of 2.5° from the beam (when the spectrograph was at 5°, Fig. 1). The charge collection in each of the Faraday cups was monitored with a fixed detector and was generally found to be reliable within the statistical error of the number of events accumulated in the monitor.

To provide a quick method of verifying the effective solid angle of the spectrograph, the absolute cross sections for inelastic excitation with 129-MeV alpha particles of the 4.4-, 7.7-, and 9.6-MeV states in ^{12}C were measured from 0° to
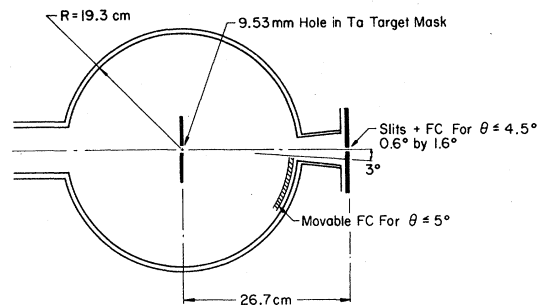
FIG. 1. Schematic drawing of the magnetic spectrograph scattering chamber illustrating the different Faraday cups (FC) that are used in different angle ranges. The Ta target mask is of sufficient width to prevent beam "halo" particles from entering the spectrograph.

40°. Over the range 6.5° to 40°, these cross sections were measured in a 91-cm scattering chamber using solid-state detectors. The experimental technique was similar to that described in Ref. 6, except that particle identification was unnecessary. Similar measurements were made from 2° to 12° with the Enge split-pole magnetic spectrograph. The solid-state detector and spectrograph measurements were normalized at five common angles. A map of the vertical distribution in the focal plane of events from ^{12}C(α, α')^{12}C* (4.44 MeV) and ^{12}C(α, ^{3}He)^{13}C which appear near opposite ends of the counter was measured to verify that the image in the focal plane was within the 1.2-cm height of the detector. To define the effective solid angle for the slit opening used at 0°, the ^{12}C yield at 9° with the large slit opening (6.4° ×3.7°) was measured and compared to that obtained by averaging the angular distribution over the 6.4° horizontal opening. The ^{12}C cross sections obtained from 0° to 40° for the 4.4- and 7.7-MeV
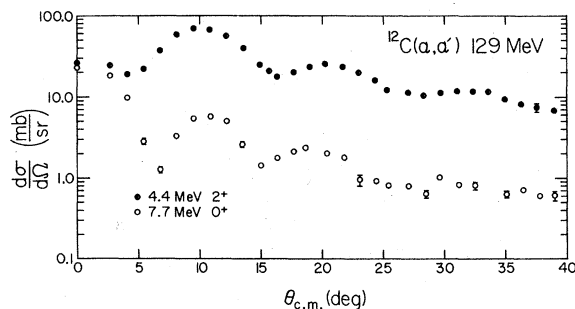
FIG. 2. The angular distributions of 4.4- and 7.7-MeV states as observed in the ^{12}C(α, α') reaction at 129-MeV incident beam energy. Error bars reflecting statistical uncertainties only are shown for a few representative points.

TABLE I. Transition probabilities (in single particle units) obtained for low lying states. $B(El)$ values were obtained in the manner described by Bernstein [a] (method II) using a Fermi matter distribution with $R_{matter} = 1.2 A^{1/3}$ fm.

Nucleus	E_α (MeV)	E_{exc} (MeV)	J^π	βR [b] (fm)	$B(El)$ [b] (spu)	$B(EL)(EM)$ [a] (spu)	$B(EL)(\alpha, \alpha')$ [a] (spu)
^{90}Zr	96	2.19	2^+	0.42	4.0	3.5 ± 1.3 6.8 ± 1.0	5.7 ± 1.7 3.7 ± 0.6
^{90}Zr	96	2.75	3^-	0.77	15.6	32.0 ± 1.0	20.0 ± 1.6
^{116}Sn	129	1.29	2^+	0.68	13.6	12.0 ± 1.6 [c]	
^{116}Sn	129	2.27	3^-	0.88	25.2	15 ± 4	24.2 ± 3.6

[a] A. M. Bernstein, Adv. Nucl. Phys. **3**, 325 (1969), unless otherwise noted.

[b] The errors are estimated to be ±15%.

[c] P. H. Stelson and F. K. McGowan, Phys. Rev. **110**, 489 (1958).

states are shown in Fig. 2. The efficiency of the detection system in the spectrograph for the 129-MeV data runs was then monitored by short (~5 min.) ^{12}C runs taken at the same angle as the data runs.

The absolute normalization of the 96-MeV ^{90}Zr(α, α') data taken over the angular range 3°–7° in the spectrograph was checked by normalizing the cross sections of the two low lying states at 2.19 MeV (2^+) and 2.75 MeV (3^-) to optical model calculations, which were in turn normalized to solid-state detector data taken over the angular range of 9° to 57° (Ref. 6). The cross sections for two low lying ^{116}Sn states (1.29 MeV 2^+ and 2.27 MeV 3^-) were similarly checked at 129 MeV. Parameters extracted for the low lying states are summarized in Table I and are in good agreement with those obtained by others.

III. EXPERIMENTAL RESULTS AND DATA ANALYSIS

Figure 3 shows the spectra taken at 0° (displayed on an energy scale) for ^{90}Zr and ^{116}Sn. The dashed line indicates the assumed shape of the continuum that was subtracted as background.

The giant resonance region of ^{90}Zr at six angles from 3° to 8° (after subtraction of the continuum) is shown in Fig. 4. Two Gaussians shown superimposed on the data were fitted to the giant resonance peak simultaneously at all angles measured using a least squares technique. The widths and excitation energies of the upper and lower peaks were varied simultaneously at all angles, while the amplitudes were varied independently. The fitting procedure used was that of Mathews and Walker.[7] Uncertainties of the peak parameters (centroid, width, and amplitude) which correspond to the variance or mean square deviation of those parameters were obtained from appropriate elements of the error matrix.

The differential cross sections obtained for ^{90}Zr are shown in Fig. 5 as a function of center of mass angle. The error bars on the data points are the mean square deviation and hence do not account for uncertainties in the choice of background. The uncertainties in the absolute cross
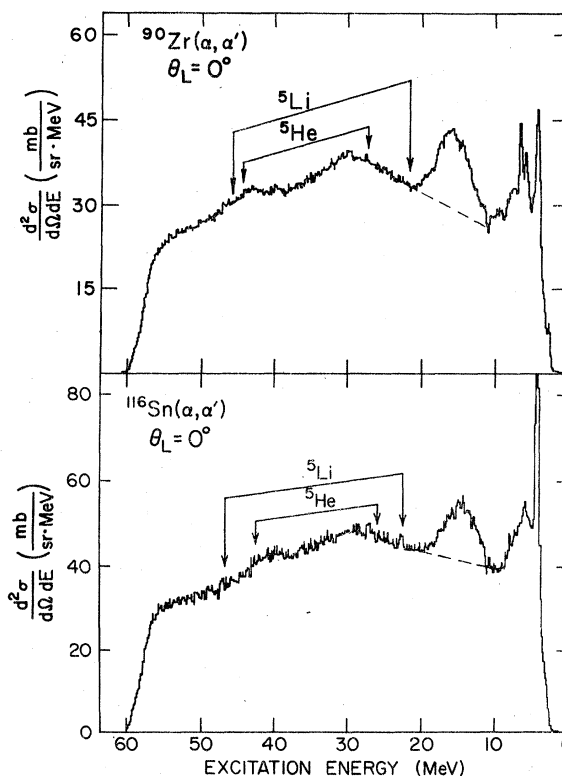
FIG. 3. Spectra of inelastically scattered α particles from ^{90}Zr and ^{116}Sn at 0°, with elastics (beam) and a few MeV of low excitation blocked by the beam stop. The dashed lines represent the assumed shape of the underlying continuum subtracted as background for peak analysis. Kinematic limits for α particles from ^{5}Li and ^{5}He breakup are shown.
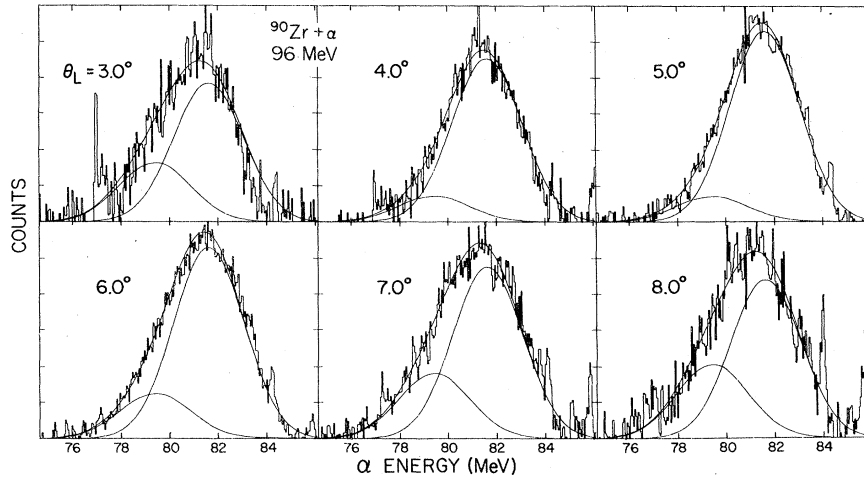
FIG. 4. Structure of the GR region in ^{90}Zr (after subtraction of the continuum) with the two-peak fits superimposed.
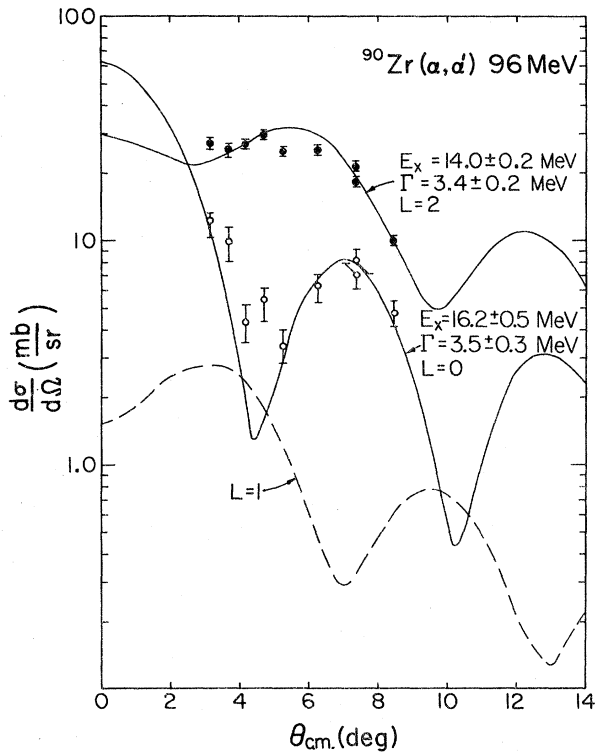
FIG. 5. Angular distributions for the two components of the giant resonance peak in ^{90}Zr obtained by a multiple spectrum fitting routine (see text). The solid dots are for the lower excitation component (GQR) while the open circles are for the higher excitation component (GMR). The error bars on the cross sections represent the statistical errors only.
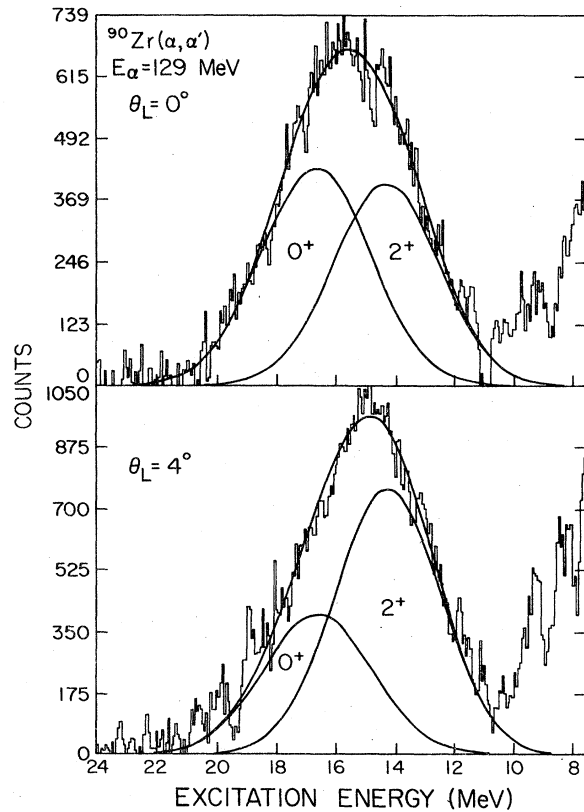
FIG. 6. Portions of the spectra of 129-MeV α particles inelastically scattered from ^{90}Zr taken at 0° and 4° after subtraction of the continuum. The solid lines indicate the GQR and GMR components and their sum for each spectrum.
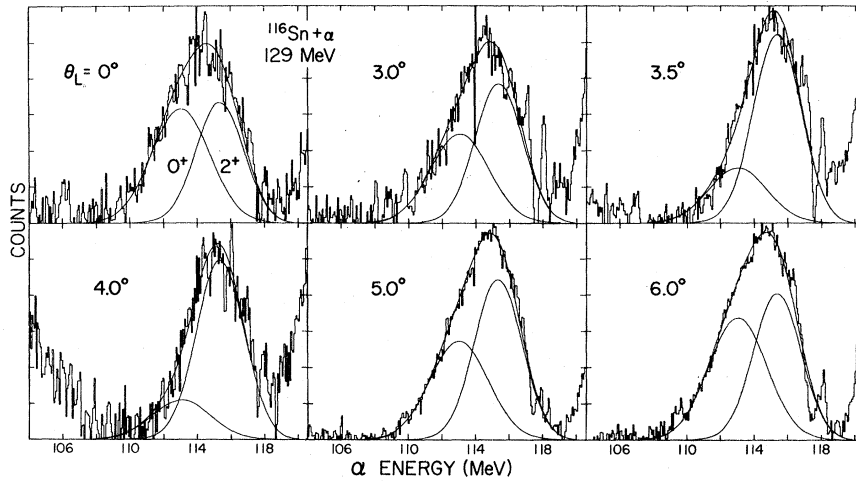
FIG. 7. Structure of the GR region in ^{116}Sn (after subtraction of the continuum) with two-component fits superimposed.

sections are quite large, ~30%, because of uncertainties in background and peak decomposition. The uncertainties given on the excitation energy and width include deviations due to the various background choices as well as uncertainties in the energy calibration. Fits to the giant resonance region of ^{90}Zr for the 129-MeV data are shown in Fig. 6 and yield peak parameters in agreement with those from the 96-MeV data. A similar analysis of the ^{116}Sn data yielded the results shown in Figs. 7 and 8.

Distorted-wave Born approximation (DWBA) calculations were made using the computer code DWUCK,[8] modified to calculate form factors for monopole and dipole transitions. The optical model parameters used were obtained from the analysis of elastic scattering data and are given in Table II. A standard collective form factor including Coulomb excitation was used for $L \geq 2$ (i.e., derivative of the optical potential). The form factor (including Coulomb excitation) suggested by Satchler[9] was used for the GDR calculations (see also Ref. 6).

The transition operator for excitation of a GMR is

$$U = U_1(r)\beta_0 Y_{00}(\Omega) .$$

Satchler[9] has obtained form factors (U_1) corresponding to two models of the GMR. The first (version I) is a compressional or breathing mode where

$$U_1 = -3U_0(r) - r \frac{dU_0(r)}{dr} .$$

$U_0 = V + iW$ is the optical model potential utilized in the entrance and exit channels. For such a monopole state located at an excitation energy E_x

which exhausts the energy weighted sum rule (EWSR),

$$\beta_0^2 R^2 = \frac{20\pi}{3A} \frac{\hbar^2}{2mE_x} .$$
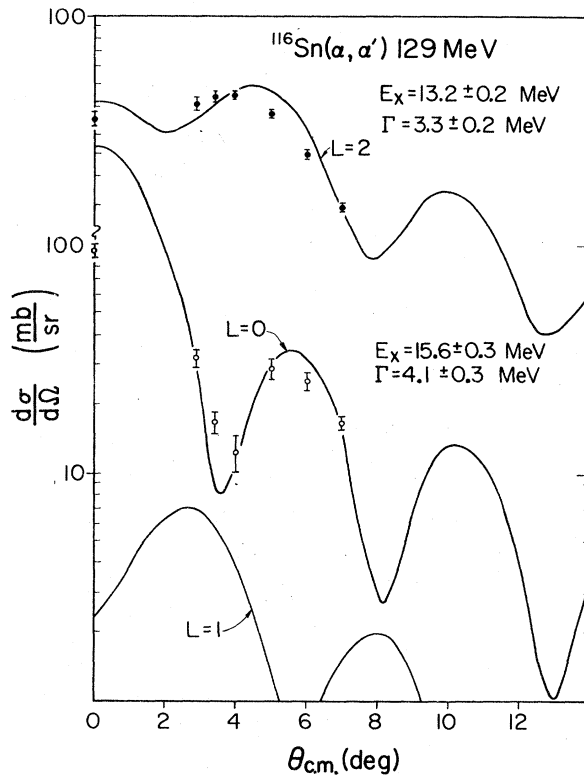
FIG. 8. Angular distributions for the two components of the giant resonance peak in ^{116}Sn obtained by a multiple spectrum fitting routine. The 0° points have been corrected for the large solid angle. See Fig. 5 caption.

TABLE II. Optical model parameters.

Nucleus	E (MeV)	V (MeV)	W (MeV)	r_0 (fm)	a_0 (fm)	r_c (fm)	Data angle range
^{90}Zr	96	45.7	27.7	1.50	0.70	1.30	(9°−57°)
^{116}Sn	129	60.8	40.9	1.40	0.73	1.35	(12°−50°)

The above form factor was used for the GMR calculations presented in this work. Satchler[9] also obtained the form factor corresponding to a deformation of the nuclear surface (version II). In this model both the form factor and EWSR (for $\beta_0{}^2$) are dependent upon the nuclear diffuseness and radius; for a uniform distribution version II reduces to version I. DWBA calculations with version II resulted in angular distribution shapes virtually identical with those of version I; predicted cross sections with version II were from 1.5 to 2.0 times smaller than those of version I.

DWBA predictions are shown superimposed on the data in Figs. 5 and 8. The lower excitation component of the giant resonance (GR) peak in both nuclei is fitted well by an $L = 2$ calculation and is the GQR. The higher excitation component, fitted well by $L = 0$, is the GMR. The calculated cross section for the GDR exhausting 100% of the EWSR is approximately an order of magnitude smaller than the observed GMR cross section. The parameters obtained for the two components of the giant resonance peak along with our current results[3] for ^{144}Sm and ^{208}Pb are summarized in Table III.

The ^{90}Zr data reported in Ref. 6 (taken from 13° to 28°) were reanalyzed assuming two peaks having the widths and energies given in Table III. The cross sections obtained for the GQR and GMR from this analysis corresponded to ~52% of the $E2$ EWSR

TABLE III. Parameters of the GMR and GQR. The errors in this table are estimates of a most probable error and are all greater than the statistical errors.

	E_{0^+} (MeV)	Γ_{0^+} (MeV)	$EA^{1/3}$ (MeV)	EWSR (%)	K_A (MeV)
^{90}Zr	16.2 ± 0.5	3.5 ± 0.3	73	90 ± 25	117 ± 4
^{116}Sn	15.6 ± 0.3	4.1 ± 0.3	76	180 ± 60	129 ± 5
^{144}Sm	14.8 ± 0.3	2.9 ± 0.2	78	85 ± 25	134 ± 5
^{208}Pb	13.7 ± 0.4	3.0 ± 0.5	81	90 ± 25	147 ± 9

	E_{2^+} (MeV)	Γ_{2^+} (MeV)	$EA^{1/3}$ (MeV)	EWSR (%)	
^{90}Zr	14.0 ± 0.2	3.4 ± 0.2	63	66 ± 20	
^{116}Sn	13.2 ± 0.2	3.3 ± 0.2	64	84 ± 25	
^{144}Sm	12.4 ± 0.2	2.3 ± 0.2	65	100 ± 30	
^{208}Pb	11.0 ± 0.2	2.7 ± 0.3	65	105 ± 30	

and ~100% of the $E0$ EWSR respectively, consistent with the small angle data. The angular distributions were not particularly well fitted at these larger angles. The GMR EWSR fraction obtained for ^{116}Sn (180 ± 60%) is somewhat outside the sum-rule limit. Although the uncertainty quoted allows for variation of both background and peak decomposition, significantly different GMR cross sections could result if the GQR peak were not Gaussian, or if it had a high energy tail. Differing sets of optical parameters also have been found to give somewhat different GMR cross sections. In any case, the accuracy of DWBA predictions for the monopole resonance has not been established as the form factors can be tested only on the GMR, and it has not been observed with other techniques.

IV. DISCUSSION

Other experimental information on the GMR is rather limited. As the GMR overlaps almost completely with the GDR, experiments which excite the GDR provide, at best, ambiguous results. Analyses of electron scattering data from Sendai have shown that for both ^{90}Zr (Ref. 10) and ^{208}Pb (Ref. 11) the GDR strength estimated from the Steinwedel-Jensen model exhausts all of the experimental strength in the region. The GDR strength estimated from the Goldhaber-Teller model is much smaller, however, and the data are nicely fitted by a combination of the GDR and the GMR exhausting essentially the full sum-rule strength. The energies and widths extracted for the GMR for ^{90}Zr and ^{208}Pb by the Sendai group agree with the results reported here. Pitthan et al.[12] studied the effects of different models for the form factor on the analysis of electron scattering data taken on ^{140}Ce and reached much the same conclusion, although they argue for the use of the Myers-Swiatecki form factor, which better reproduces the mass dependence of the GDR energy and leaves little room for a monopole contribution. Further work is clearly needed before estimates of the GDR strength in electron scattering can be done with sufficient reliability to allow extraction of properties of the underlying GMR.

In a reanalysis of existing (p, p') data, Bertrand

et al.,[13] utilizing recent estimates of the isovector part of the proton-nucleus interaction, have shown that their published (p, p') data are consistent with a GMR at approximately the position of the GDR in ^{208}Pb, ^{144}Sm, ^{120}Sn, ^{90}Zr, and several other nuclei. The energies and widths extracted agree with those from this study (within the errors) except for ^{90}Zr, where the energy of Bertrand et al. is slightly higher. As they must subtract the GDR contribution and work with data having relatively poor statistical accuracy, their uncertainties are quite large.

The incompressibility K_{nm} (or compression modulus) of nuclear matter is defined by[1]

$$K_{nm} = k_f^2 \frac{d^2}{dk_f^2}\left(\frac{E}{A}\right) . \tag{1}$$

The compressibility χ is then related to the K_{nm} by

$$\chi = \frac{9}{\rho K_{nm}}, \tag{2}$$

where ρ is the density of nuclear matter. For a finite nucleus the incompressibility can be defined similarly as[1]

$$K_A = r_0^2 \frac{d^2(E/A)}{dr_0^2} , \tag{3}$$

where r_0 is the root-mean-square radius.

The incompressibility of a finite nucleus differs from that of nuclear matter by surface, Coulomb, and symmetry effects. Using the Weizsacker expression for E/A in Eq. (3), K_A can be parametrized as

$$K_A = K_{vol} + K_{surf} A^{-1/3} + K_{sym}\left(\frac{N-Z}{A}\right)^2 + K_{Coul} , \tag{4}$$

where K_{vol} corresponds to K_{nm}. The coefficients in Eq. (4) can be viewed as second derivatives with respect to r of corresponding coefficients in the mass equation. Unfortunately, the derivatives of the coefficients in the mass equation cannot be evaluated with sufficient accuracy to obtain meaningful estimates of K_{surf}, K_{sym}, and K_{vol} (or K_{nm}).

K_A can be related to the energy of the GMR by[1,2]

$$E_m = \hbar/r_0(K_A/m)^{1/2} , \tag{5}$$

where r_0 is the root-mean-square nucleon radius (taken to be $0.96A^{1/3}$ fm) and m is the nucleon mass.

Another commonly used relationship between the breathing mode energy and the incompressibility is that obtained for a liquid drop. Imposing the boundary condition that the change in density at the surface vanishes, the energy of the lowest compression made of a liquid drop can be related to the compression modulus K by[14]

TABLE IV. Coefficients of the terms in the liquid drop expression for compressibility (MeV).

	Exp [a]	PA [b]	B1 [c]	D1 [c]	SKA [c]	SIV [c]	SIII [c]
K_{vol}	236	240	190	228	263	325	356
K_{surf}	-550	-533	-300	-315	-394	-513	-568
K_{sym}		-526	-500	-500	-610	-580	-630

[a] The errors on K_{vol} and K_{surf} terms are estimated to be 10% and 25%, respectively. The K_{sym} term is small, almost negligible, and hence cannot be determined. The data are equally well fitted by K_{sym} in the range 0 to -850.

[b] This is a fit to the K_A values calculated from the excitation energies of Ref. 15 by the same procedure as the column marked Exp.

[c] Reference 1.

$$E_m = \frac{\hbar}{R_0}\left(\frac{\pi^2}{9}\frac{K}{m}\right)^{1/2} = \frac{\hbar}{r_0}\left(\frac{\pi^2}{15}\frac{K}{m}\right)^{1/2} , \tag{6}$$

where R_0 is the equilibrium radius of the liquid drop and is related to the root-mean-square radius $r_0^2 = \frac{3}{5}R_0^2$. For heavy nuclei K obtained from expression (6) is close to K_{nm}. By comparison of Eqs. (5) and (6), it is clear that $K = (15/\pi^2)K_A = 1.52K_A$; one must be careful to specify which incompressibility is being used. The values for K_A obtained from the present data are summarized in Table III. Taking $K_{Coul} = \frac{6}{5}Z^2e^2/r_c A^{4/3}$ with $r_c = 1.24A^{1/3}$ fm, Eq. (4) was fitted to the values of K_A in Table III in an attempt to estimate the coefficients in (4) from the A dependence of K_A. The results of the best fit obtained to the calculated K_A are given in Table IV, the resulting $K_{nm} \approx 236$ MeV. These results are in agreement with the predictions of Pandharipande,[15] where the values
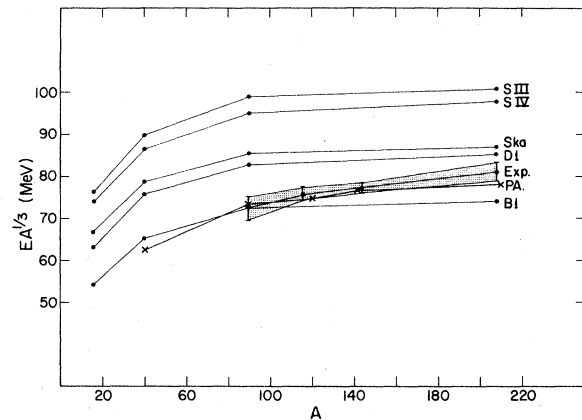
FIG. 9. Plot of the experimental values for the excitation energy of the GMR times $A^{1/3}$ versus A (dotted area). Also shown are various RPA predictions. Symbols are the same as those in Table IV.

in the table are the results of our fit to his re-
normalized data with the symmetry term included.
Bohigas et al.[2] show that the incompressibility
of nuclear matter can be approximately related to
that of a finite nucleus by $K_{nm} \approx K_A + 63\ (\gamma + 1)$ MeV,
where γ is the value of the power in the density de-
pendence of a Skyrme type force. Investigating
these properties, they have shown that the ener-
gies of the GQR and GMR can be reproduced if
the value of γ is reduced from $\gamma = 1$ (for a pure
Skyrme) to $\gamma \approx \frac{1}{3}$. The value of K_{nm} obtained in this
fashion from the data is $K_{nm} \approx 215$ MeV.

In Fig. 9, the experimental values for the energy
(E) of the GMR times $A^{1/3}$ for Zr, Sn, Sm, and
Pb are plotted with respect to A along with the
results of various RPA calculations of Blaizot
et al.[1] The data points lie in the region of the
finite range predictions of the $B1$ and $D1$ interac-
tions resulting in $K_{nm} \approx 200$ MeV, well below the
predictions of the pure Skyrme type interactions.
Although the errors are relatively large, the pre-
dicted A dependence of the GMR energy does not
appear to follow the data. The A dependence of
$EA^{1/3}$ for the GMR is well reproduced by the re-
sults of Pandharipande.[15]

It is clear that additional experiments are nec-
essary to establish more accurately the param-
eters of the GMR. Particularly, knowledge of its
location in lighter nuclei would permit a better
determination of the mass dependence of the in-
compressibility; comparisons of experimental
results from several reactions should better es-
tablish its strength.

ACKNOWLEDGMENTS

[1]J. P. Blaizot, D. Gogny, and B. Grammaticos, Nucl.
Phys. <u>A265</u>, 315 (1976).
[2]O. Bohigas, A. M. Lane, and J. Martorell, Phys. Rep.
<u>51</u>, 267 (1979).
[3]D. H. Youngblood, C. M. Rozsa, J. M. Moss, D. R.
Brown, and J. D. Bronson, Phys. Rev. Lett. <u>39</u>, 1188
(1977).
[4]G. F. Trentelman and E. Kashy, Nucl. Instrum. Meth-
ods <u>82</u>, 304 (1970).
[5]F. G. Resmini, A. D. Bacher, D. J. Clark, E. A.
McClatcher, and D. R. Swiniarski, Nucl. Instrum.
Methods <u>74</u>, 261 (1969).
[6]D. H. Youngblood, J. M. Moss, C. M. Rozsa, J. D.
Bronson, A. D. Bacher, and D. R. Brown, Phys. Rev.
C <u>13</u>, 994 (1976).
[7]J. Mathews and R. L. Walker, *Mathematical Methods
of Physics*, 2nd ed. (Benjamin, New York, 1970),
p. 387.
[8]Received from P. D. Kunz, University of Colorado.
[9]G. R. Satchler, Part. Nucl. <u>5</u>, 195 (1973); Nucl. Phys.
<u>A195</u>, 1 (1972).
[10]S. Fukuda and Y. Torizuka, Phys. Lett. <u>62B</u>, 146
(1976).
[11]M. Sasao and Y. Torizuka, Phys. Rev. C <u>15</u>, 217
(1977).
[12]R. Pitthan, H. Hass, D. H. Meyer, J. N. Dyer, and
F. R. Buskirk, Phys. Rev. Lett. <u>41</u>, 1276 (1978).
[13]F. E. Bertrand, G. R. Satchler, D. J. Horen, and
A. van der Woude, Phys. Lett. <u>80B</u>, 198 (1979); Phys.
Rev. C <u>18</u>, 2788 (1978).
[14]A. Bohr and B. Mottelson, *Nuclear Structure* (Benja-
min, New York, 1975), Vol. 2, p. 666.
[15]V. R. Pandharipande, Phys. Lett. <u>31B</u>, 635 (1970).